Supporting Information

Ultra-low lattice thermal conductivity driven high thermoelectric figure of merit in Sb/W co-doped GeTe

Khasim Saheb Bayikadi[1], Safdar Imam[1], Wei-Shen Tee[2], Sugumaran Kavirajan[1], Chiao-Yu Chang,[2] Amr Sabbah,[2,3] Fang-Yu Fu,[4] Ting-Ran Liu,[4] Ching-Yu Chiang [5], Dinesh Shukla[6], Chien Ting Wu[7], Li-Chyong Chen[4,8], Mei-Yin Chou[2]*, Kuei-Hsien Chen[2,4]*, Raman Sankar[1]*

[1]Institute of Physics, Academia Sinica, Nankang, Taipei, Taiwan 11529
[2]Institute of Atomic and Molecular Sciences, Academia Sinica, Taipei 10617, Taiwan
[3]Tabbin Institute for Metallurgical Studies, Tabbin, Helwan 109, Cairo 11421, Egypt
[4]Center for Condensed Matter Sciences, National Taiwan University, Taipei 10617, Taiwan
[5]National Synchrotron Radiation Research Center, Hsinchu city 30077, Taiwan
[6]UGC-DAE Consortium for Scientific Research, Indore 452001, India
[7]Taiwan Semiconductor Research Institute, Hsinchu Science Park, Hsinchu 300, Taiwan
[8]Center of Atomic Initiative for New Materials, National Taiwan University, Taipei 10617, Taiwan

Formation energy

The *ab initio* method was used to study the formation energies of the W-doped GeTe systems. The formation energy of a defect is defined as follows:

$$E^f[\mathrm{X}] = E_{tot}[\mathrm{X}] - E_{tot}[X_0] - \sum_i n_i\mu_i,$$

where $E_{tot}[\mathrm{X}]$ is the total energy derived from a supercell calculation with one defect in the cell, $E_{tot}[X_0]$ is the total energy for the equivalent supercell containing no defects, n_i is the number of atoms of type *i* added to ($n_i > 0$) or removed from ($n_i < 0$) the supercell when the defect is created, and μ_i is the corresponding chemical potential of species *i*. For simplicity, the total energies (per atom) of the bulk were used as the chemical potentials. For example, the formation energies of substitution W (denoted as W^s) and interstitial W (denoted as W^i) were calculated as follows:

$$E^f[W^s] = E_{tot}[W_1Ge_{26}Te_{27}] - E_{tot}[Ge_{27}Te_{27}] + E[Ge_{bulk}] - E[W_{bulk}];$$

$$E^f[W^i] = E_{tot}[W_1Ge_{27}Te_{27}] - E_{tot}[Ge_{27}Te_{27}] - E[W_{bulk}].$$

The formation energies of each defect (W^s and W^i) were calculated for both cubic and rhombohedral phases. As Ge-vacancies readily form in GeTe[1] and GST compounds[2], the formation energies of W atoms in the presence of a Ge vacancy in the supercell were also considered. Two interstitial positions were considered, as shown in **Figure S1**. Furthermore, substitution W can go to the vacancy site or a Ge site. The calculated results for both cubic and rhombohedral phases are summarized in **Table 1**. These results show that the formation energy of W doping to GeTe was quite high, at ~3 eV. However, if a vacancy was present in the system, the formation energy could decrease to ~2 eV, indicating that the presence of vacancies was beneficial to W doping. These formation energies were comparable to those of Sb_2Te_3[3]

Notably, a study of the reactivity of different transition metals with GeTe showed that W was belonged to the un reactive group[4]. However, some previous reports have indicated that W atoms can enter GeTe[5], GeSbTe[6], and Sb_2Te_3 thin-film samples using the sputtering method[3]. The formation of a Ge vacancy in the presence of a W atom in GeTe was further investigated. The calculated results for a 3×3×3 supercell is summarized in **Table 2**. From these energetic results, W-doping was concluded to facilitate the creation of more Ge vacancies, resulting in increased p-type doping. **Figure 3** shows the density of states (DOS) for cubic GeTe systems calculated using the 3×3×3 supercell. For both W^s and W^i doping, the W atom introduced additional states into the GeTe bandgap. As W^s and W^i facilitate the formation of additional Ge vacancies, based on the energetic results shown in **Table 2**, the actual Fermi level of these doped systems was lowered into the valence band.

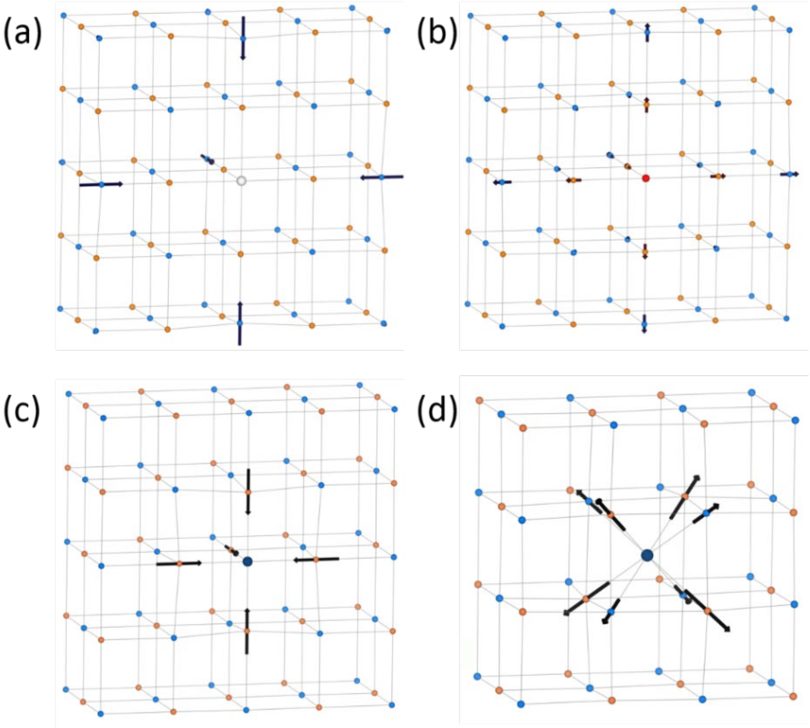

Figure S1: Structural relaxation of c-GeTe containing (a) one Ge vacancy, (b) one Sb substitution atom, (c) one W substitution atom (W^s), and (d) one interstitial W atom (W^i). Light-blue, orange, white, red, and deep-blue spheres represent Ge atoms, Te atoms, Ge vacancies, Sb atoms, and W atoms, respectively. Arrows represent the displacement of neighbouring atoms by the Ge vacancy, Sb, W^s, and W^i.

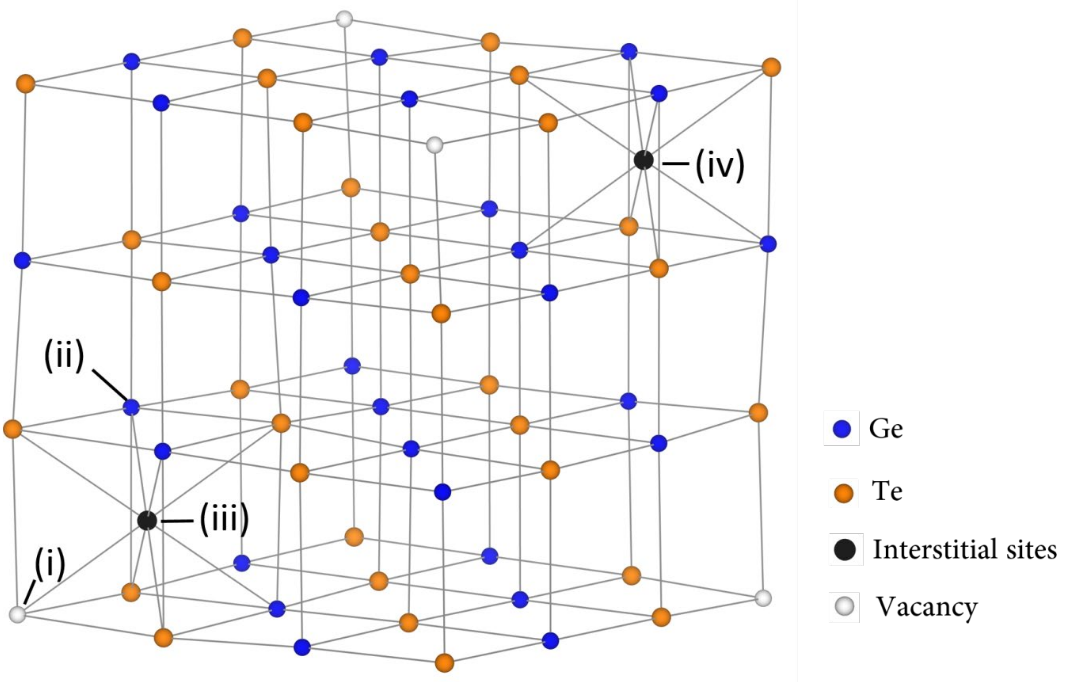

Figure S2: *Illustration of four possible positions considered for W doping: (i) Filling of the Ge vacancy, (ii) Ge site substitution, (iii) W interstitial nearest the Ge vacancy, and (iv) an interstitial site far from the Ge vacancy.*

Local relaxations resulting from Ge vacancies, Sb substitution, W substitution, and W interstitial atoms were also investigated (shown in **Figure S1**). These defect geometries have been found to induce local strain in GeTe, which might lead to perturbations in lattice dynamics and microstructures. As the six Te atoms closest to a Ge vacancy are electron-deficient, they tend to take electrons from Ge atoms, pulling these Ge atoms 0.18 Å toward Te, as shown in **Figure S1(a)**. As Sb (Sb^s) has one extra valence electron compared with Ge and is larger in size, it generates a scattering centre that drives all surrounding atoms outward, as shown in **Figure S1(b)**. **Figure S1(c)** shows how W substitution (W^s) attracts six nearby Te atoms, resulting in a displacement of 0.19 Å, indicating that W^s forms bonds with surrounding Te atoms[8]. After relaxation, the eight atoms close to the interstitial W atom (W^i) are pushed outward, with a displacement of 0.21 Å for Te atoms and 0.12 Å for Ge atoms, as shown in Figure S1(d). We also studied the relaxation profile of Ge vacancy plus Sb^s (V+ Sb^s) and Ge vacancy plus W^s (V+ W^s) at several separation distances; the combined displacement results are similar to their corresponding superposition. As the experimental investigation progressed, theoretical assessments were followed by experimental evidence of possible W doping states in GeTe. The probable W-occupied locations in the GeTe system are shown in **Figure S2**. All feasible formation energies of W substitution (W^s) and interstitial (W^i) locations in cubic and rhombohedral structures were computed, as shown in **Table 1** (no vacancy and Ge vacancy case) and explained.

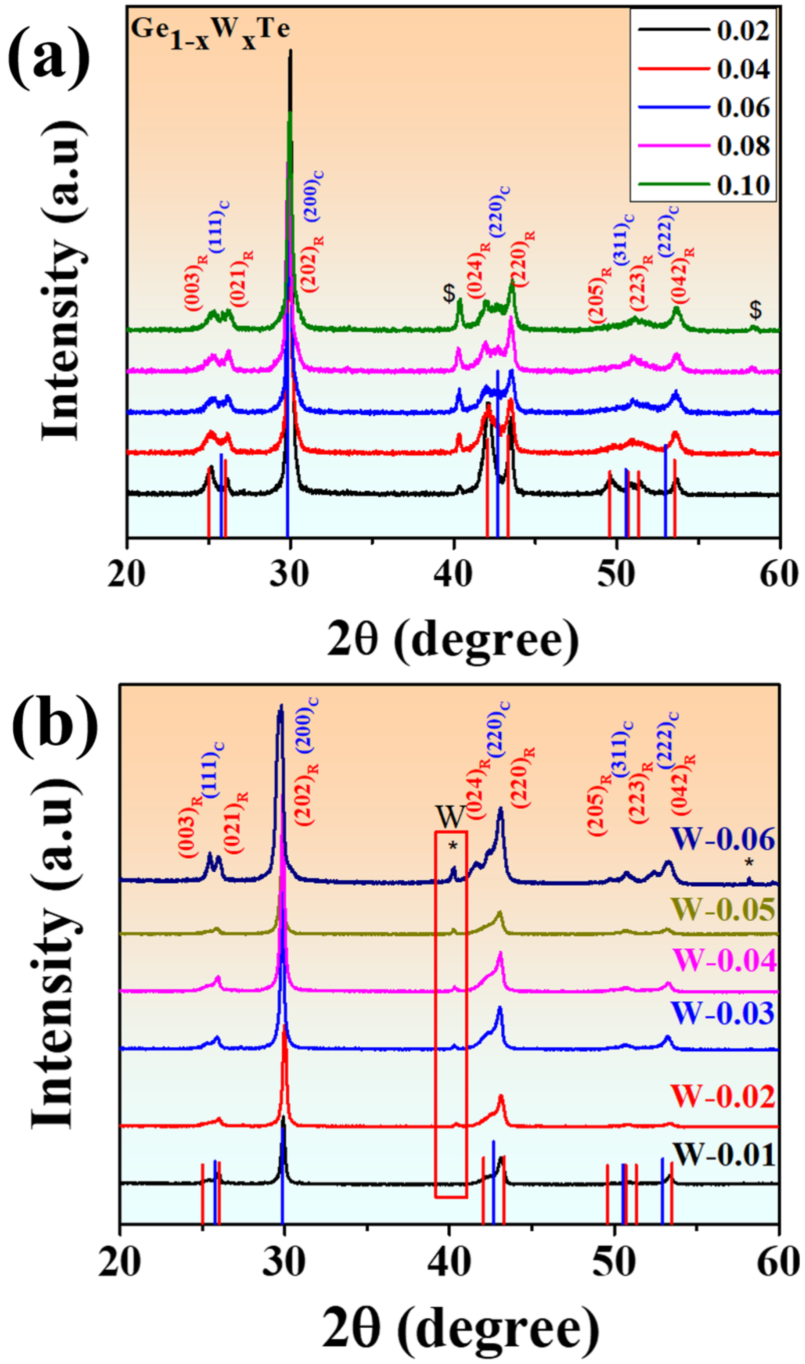

Figure S3: *(a) Powder X-ray diffraction patterns of W-doped* $Ge_{1-x}W_xTe$ *(x = 0.02–0.1) compounds, and (b) PXRD patterns of W-codoped* $Ge_{0.9-x}Sb_{0.1}W_xTe$ *compounds (x =0.01–0.06). W secondary phase peaks are represented by (*)*

Figure S3 shows the PXRD results for the W-doped GeTe compounds, with a structural change in GeTe observed with an increasing W content. From X-ray diffraction patterns of $Ge_{1-x}W_xTe$, we know that the cubic phase ($Fm\overline{3}m$) appears and the GeTe lattice is intact, indicating that W enters the GeTe lattice along with W nanoprecipitation form as a secondary phase. Individual peaks between 40° and 45°(2θ), as shown in **Figure S3**, demonstrated the rhombohedral structure of GeTe, and a single peak indicated the cubic phase[9]. The PXRD patterns of W co-doped $Ge_{0.9-x}Sb_{0.1}W_xTe$ samples are shown in **Figure S3(b)** and resemble the pseudo-cubic structure of the GeTe compounds (indexed). A regular increase in the W secondary phase occurred with increasing W concentration from $x = 0.02$ to 0.05, while further increases in W ($x = 6\%$) dramatically enhanced the W peak intensity. The Scherrer equation ($n\lambda = 2d\sin\theta$) was used to estimate the size of W secondary phase crystallites, which was ~15–25 nm. The corresponding phase distribution was further confirmed by the Grazing-incidence wide-angle X-ray scattering (GIWAXS) measurement (**Figure S4**). The W scattering low intensity circle can be observed in $Ge_{0.85}Sb_{0.1}W_{0.05}Te$, indicating the presence of W nanoprecipitate form, which is consistent with the PXRD data. Also, a systematic Rhombohedral to Pseudo cubic phase change was with Sb and W doping in GeTe compound. Consequently, small shift was observed after W doping for the $Ge_{0.85}Sb_{0.1}W_{0.05}Te$ sample, indicating which might be due to the substitution doping of W into $Ge_{0.9}Sb_{0.1}Te$ lattice.

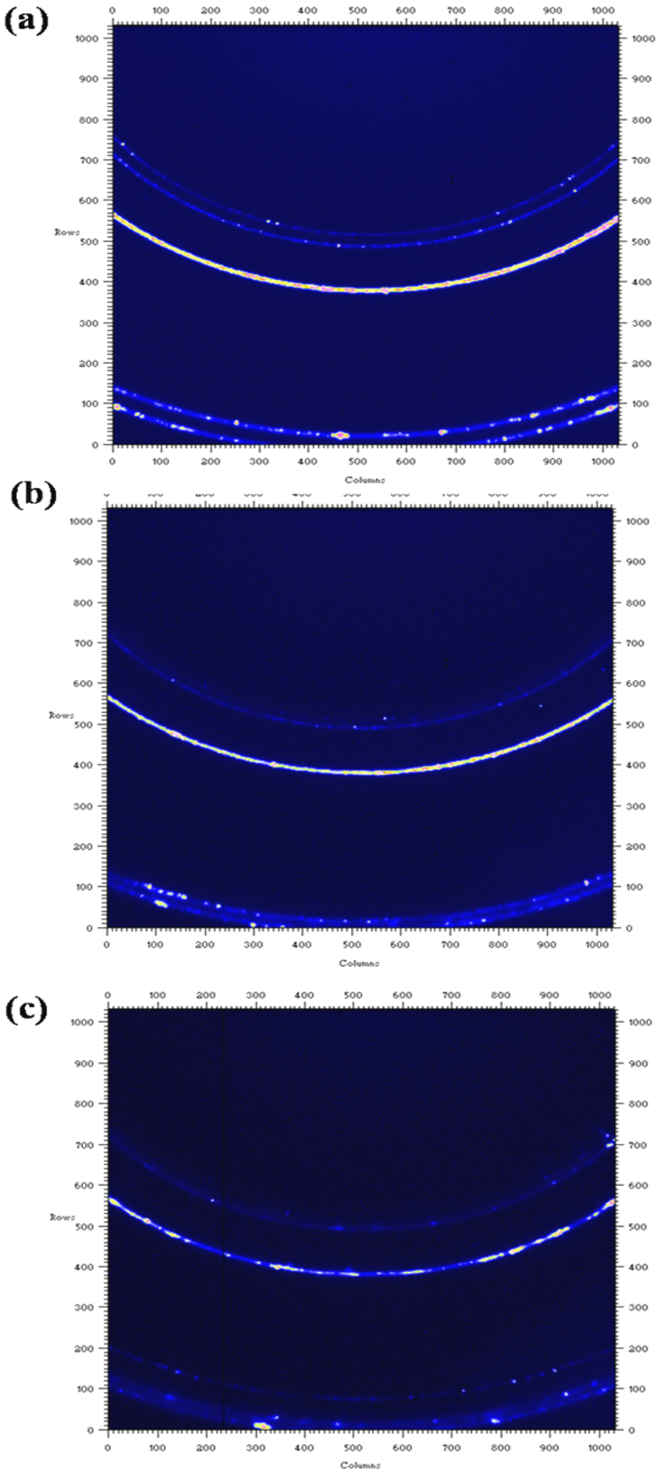

Figure S4. GIWAXS of the (a) pristine GeTe, (b) $Ge_{0.9}Sb_{0.1}Te$, and (c) $Ge_{0.85}Sb_{0.1}W_{0.05}Te$ samples.

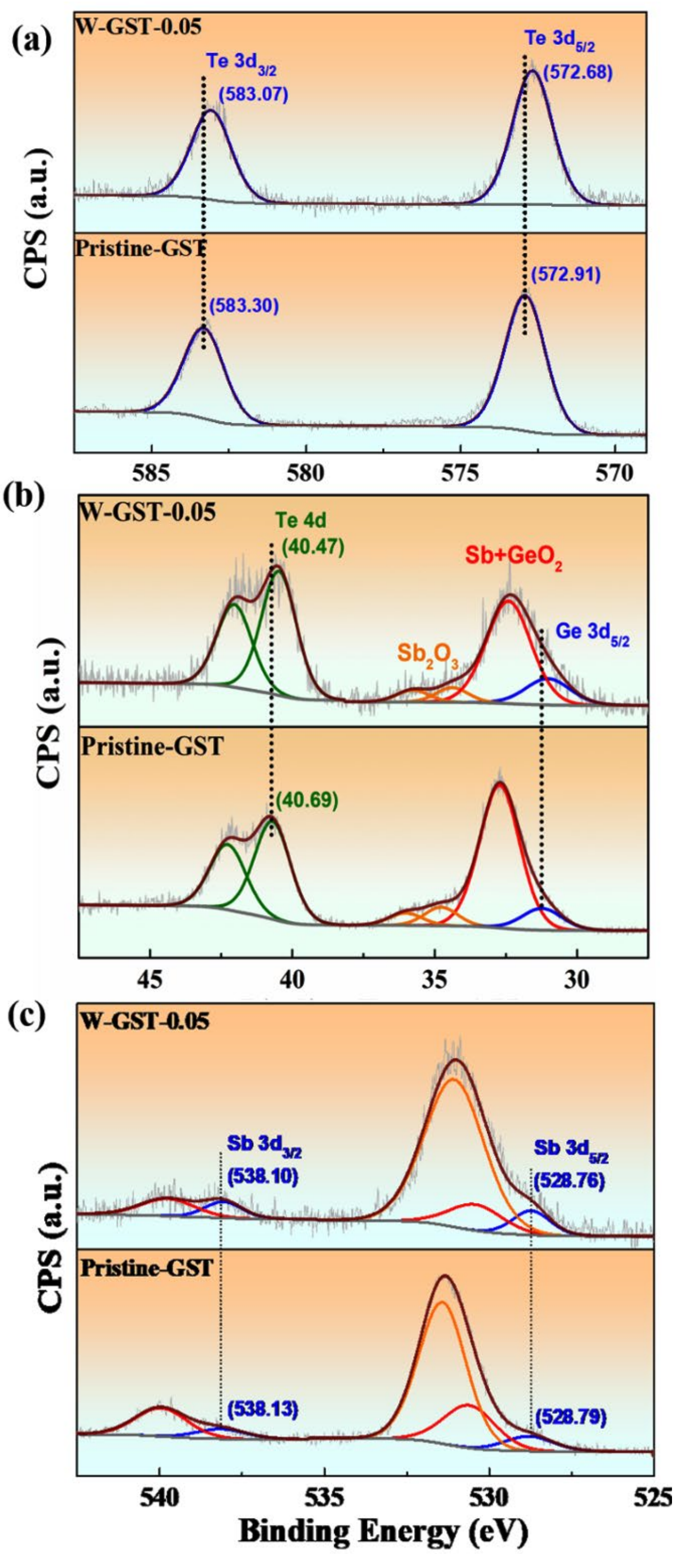

Figure S5. (a) Te 3d XPS spectrum, (b) Te 4d spectrum, and (c) Sb 3d spectrum for $Ge_{0.9}Sb_{0.1}Te$ *and* $Ge_{0.85}Sb_{0.1}W_{0.05}Te$ *respectively.*

X-ray absorption spectroscopy has demonstrated that Tungsten doping was expected to shorten the bond length between W and Te atoms[5]. This is consistent with previous models, W doping was expected to shorten the bond length between W and Te atoms, affecting the lattice dynamics. As a result, detailed investigation of the effect of W atoms on GeTe is necessary. XPS can show the chemical environment of W and Te atoms in detail. After heat-pressing and fine polishing, XPS spectra of $Ge_{0.9}Sb_{0.1}Te$ (GST) and $Ge_{0.85}Sb_{0.1}W_{0.05}Te$ (W-GST-0.05) pellets were collected, as shown in **Figure S5**. In **Figure S5(a)**, the binding energy shifts to a lower energy (0.23 eV), showing that Te ($3d^{3/2}$ and $3d^{5/2}$) was bound to W and that W occupied the Ge site[5]. Owing to the high electronegativity of W compared with that of Ge and Sb, the decreased binding energy indicated that electrons were drawn from Te by W[8]. **Figure S5(b)** shows the Te 4d states, and the lower energy peak shift (0.22 eV) induced by W doping, in addition to some surface-oxidized Ge and Sb peaks in the scans of both pristine and W-doped GST[3]. Both Sb BE **Figure S5(c)** and Ge BE have been measured repeatedly, and no discernible shifts in binding energy have been found, with the potential exception of a widening of the peak attributed in Ge owing to the existence of oxidation peaks[10].

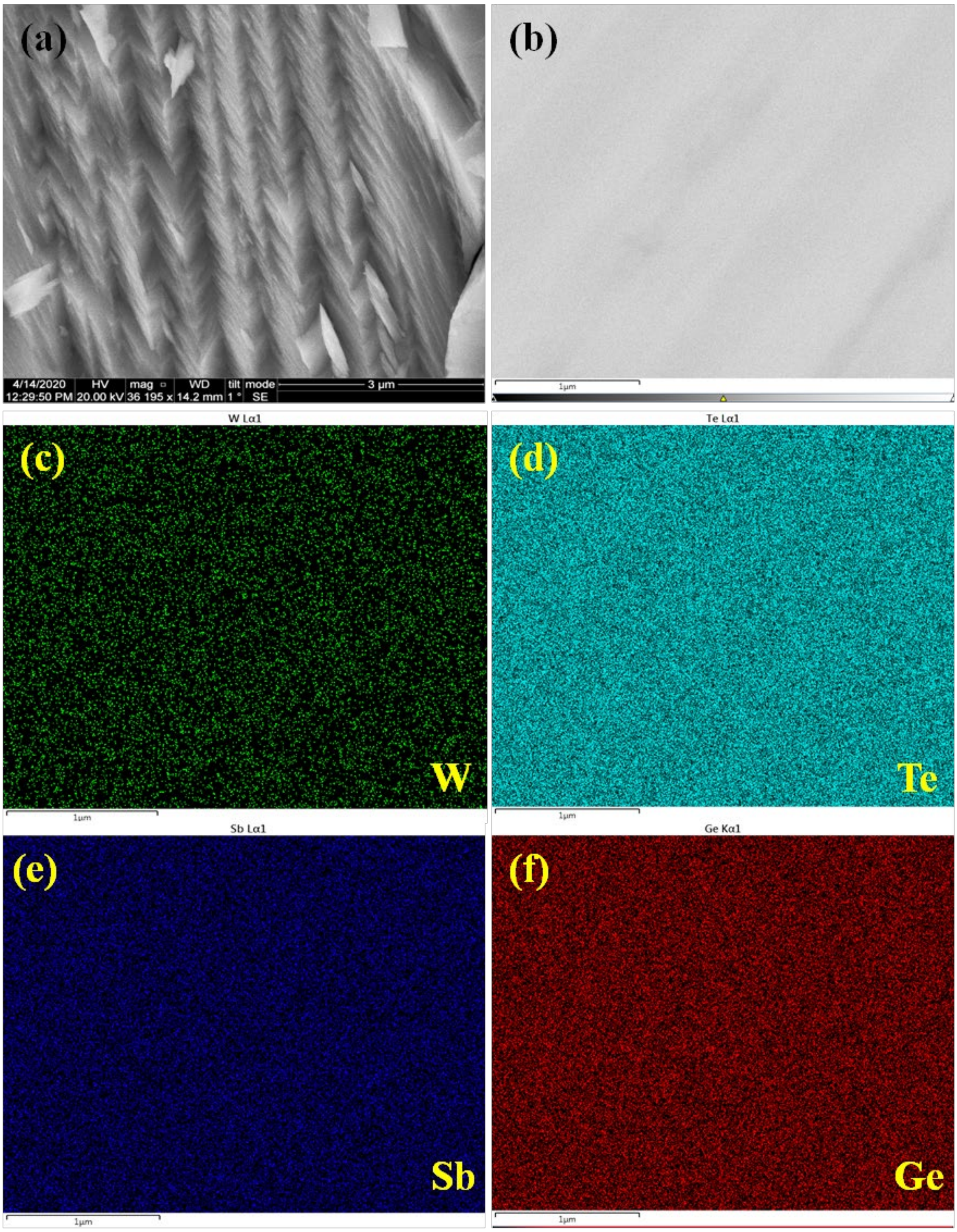

Figure S6. (a) SEM cross-sectional image of $Ge_{0.85}Sb_{0.1}W_{0.05}Te$ *pellet, (b) polished surface of the pellet for EDAX mapping, and (c) W, (d) Te, (e) Sb, and (f) Ge mappings, respectively*

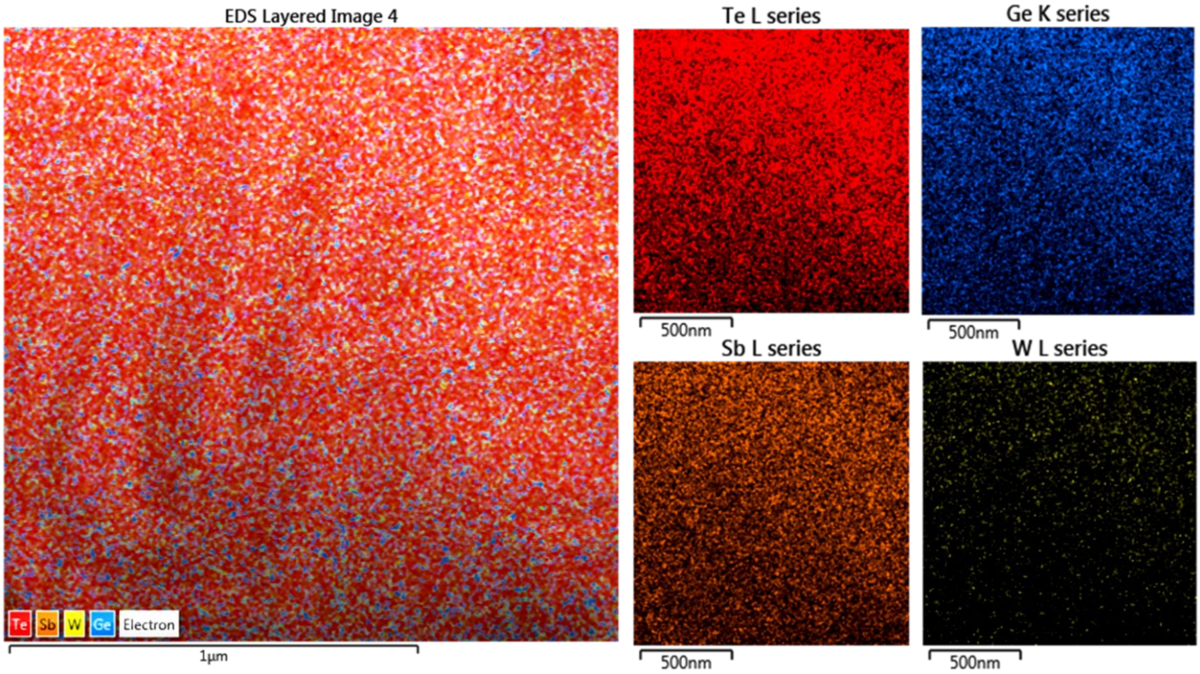

Figure S7:

Figure S7.TEM microstructure of the $Ge_{0.85}Sb_{0.1}W_{0.05}Te$ *sample and the corresponding elemental mapping of Te, Ge, Sb, and W.*

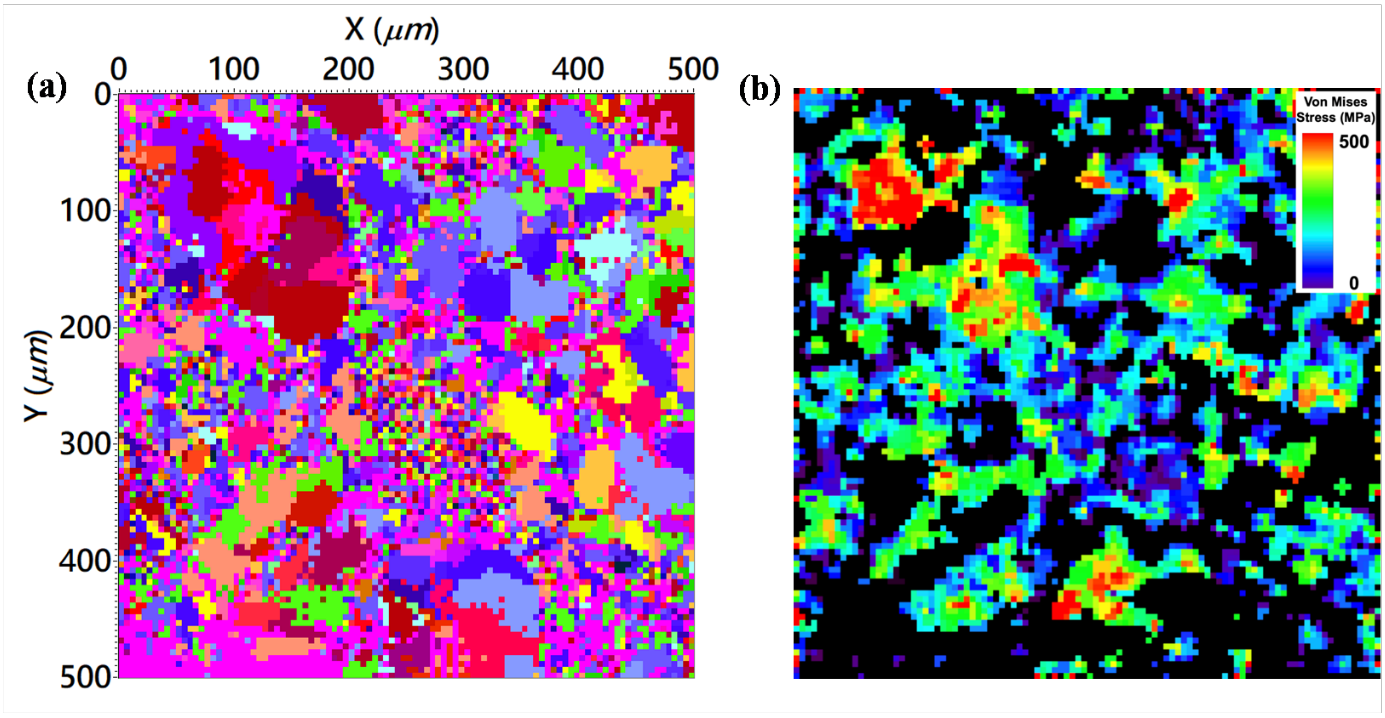

Figure S8. (a) Orientation mapping of the SEM image, and (b) von Mises stresses (MPa) in the $Ge_{0.85}Sb_{0.1}W_{0.05}Te$ sample.

FE-SEM and TEM EDAX mapping have been used to validate elemental compositions and distributions at micro- and nanoscale levels. **Figure S6(a)** shows the cross-sectional FE-SEM herring bone structure of the $Ge_{0.85}Sb_{0.1}W_{0.05}Te$ sample, and **Figure S6(b)** shows microscopic images of the fine polished pellets. **Figures S6(c)–S6(f)** show the elemental mapping of W, Te, Sb, and Ge distributions in the $Ge_{0.85}Sb_{0.1}W_{0.05}Te$ sample, confirming that all elements were uniformly distributed throughout the sample in the microscale range. The TEM image of the $Ge_{0.85}Sb_{0.1}W_{0.05}Te$ sample is shown in **Figure S7**, with elemental mapping at the 500-nm scale showing a uniform distribution. Owing to the lack of Ge and W clusters in the elemental mappings, W might have mostly located in the interstitial region or in the nanoprecipitate form. The $Ge_{0.85}Sb_{0.1}W_{0.05}Te$ sample's inverse plane mapping is shown in Figure S8(a), and it resembles a sizable polycrystalline distribution. Due of the vast microstructural dispersion and nanoprecipitation of the (W), which form a large strain distributed lattice network, **Figure S8(b)** illustrates the von Mises stress strain distribution (0 to 500 MPa).

Figure S9 shows strain boundaries in the herringbone structure, which are generated by two types of strains, namely, lattice expansion generated by Sb replacement and lattice shrinkage caused by W replacement (**Figure 5**). The scanning transmission electron microscope - high-angle annular dark-field (STEM-HAADF) image of the herringbone structure with highly strained boundaries is shown in top inset of **Figure S9**, while the bottom inset shows the magnified domain boundaries and existing strains of compound $Ge_{0.85}Sb_{0.1}W_{0.05}Te$. **Figure 6** shows high resolution images of compound $Ge_{0.85}Sb_{0.1}W_{0.05}Te$.

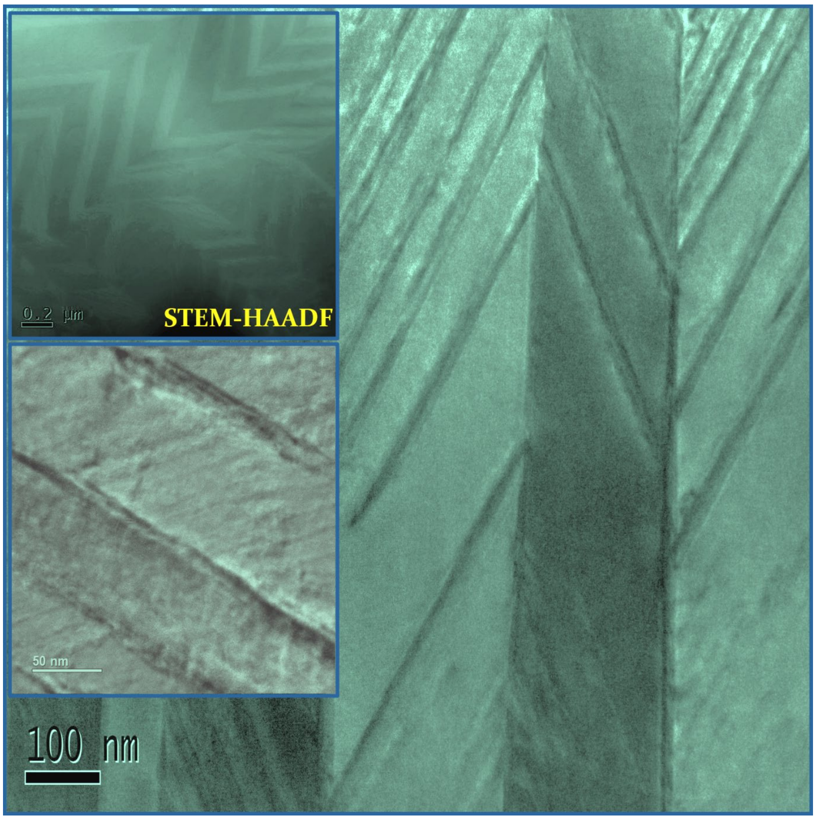

Figure S9. Structural domain strain in the herringbone structure. Top inset shows the STEM-HAADF dark field image of highly strained boundaries, and bottom inset shows the magnified view of highly strained domain boundaries.

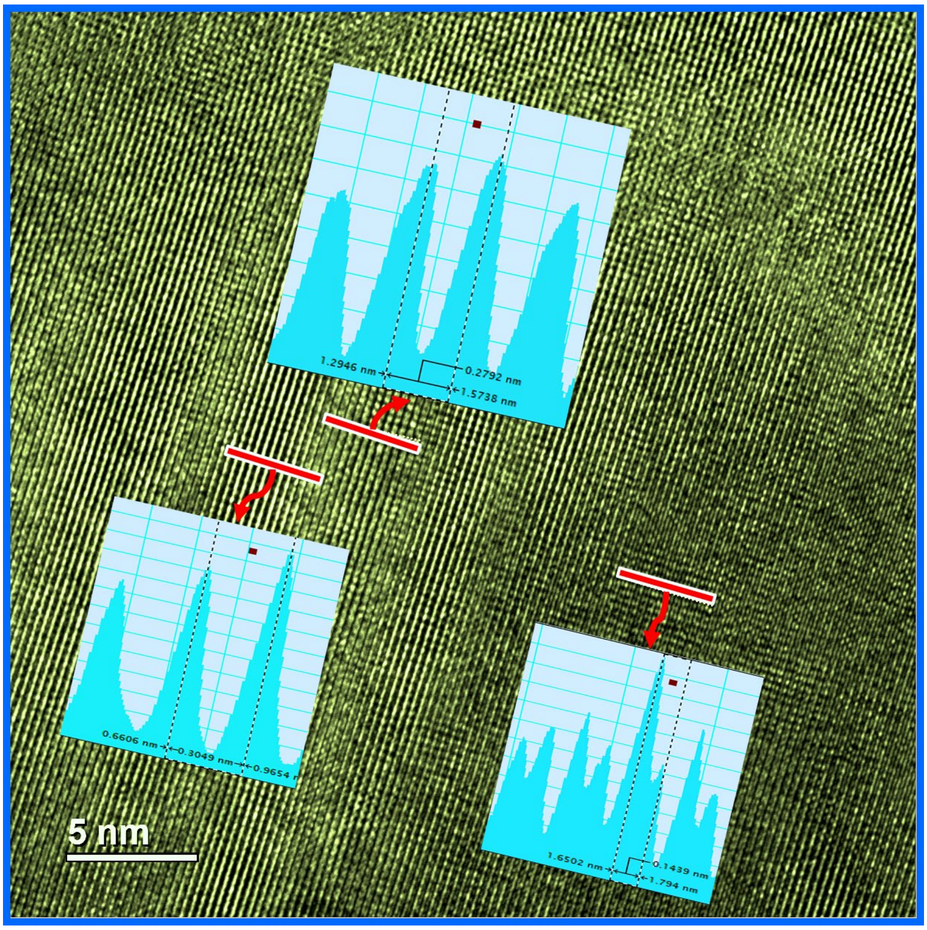

Figure S10. High resolution transmission image of the herringbone domain with different lattice displacements. Inset shows three different lattice distances in the domain

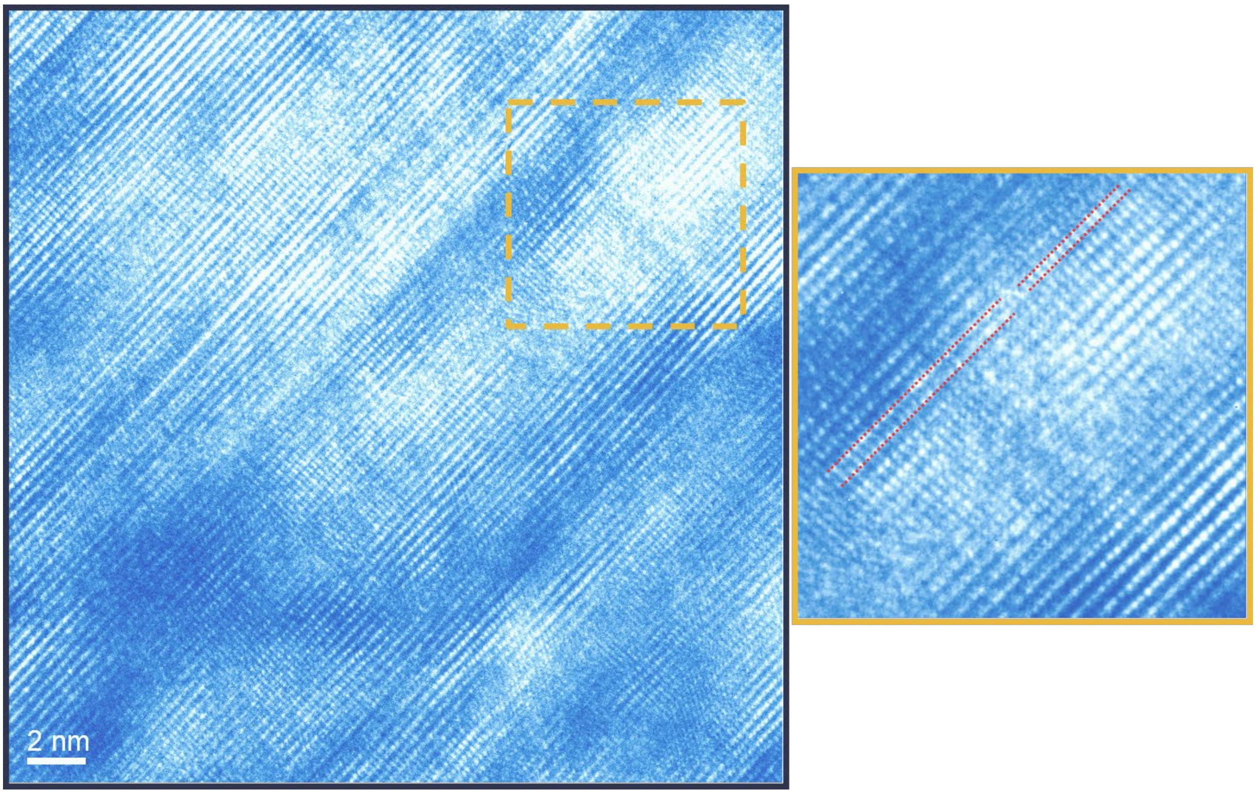

Figure S11. Lattice disorders of compound $Ge_{0.85}Sb_{0.1}W_{0.05}Te$ *indexed in the red square box, and an enlarged view of lattice merging and displacement.*

.

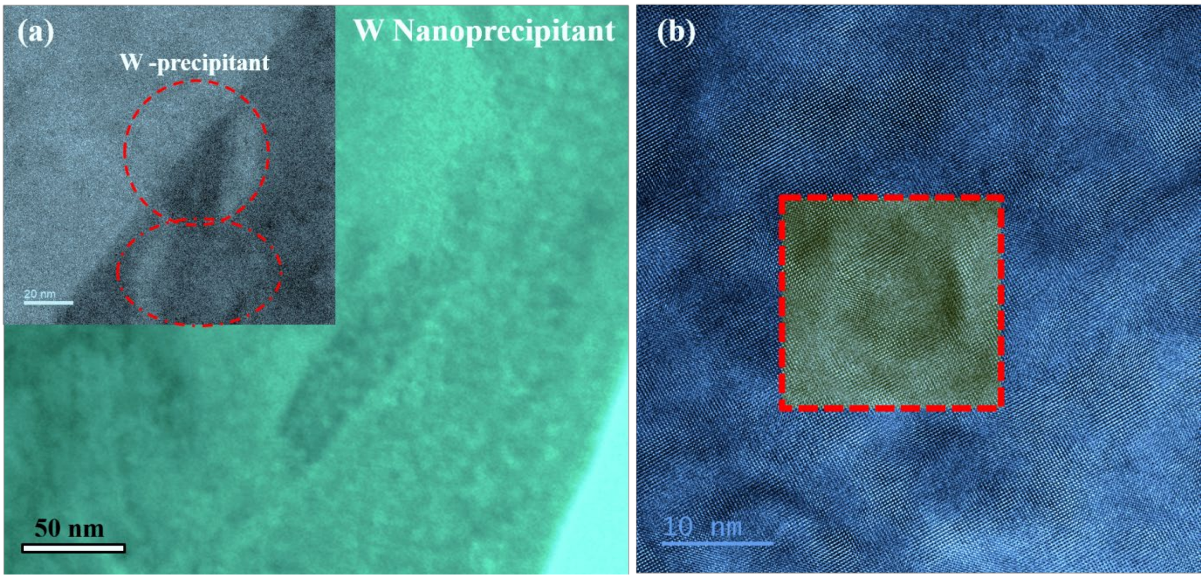

Figure S12. (a) Tungsten (W) nanoprecipitates of compound $Ge_{0.85}Sb_{0.1}W_{0.05}Te$ *(inset, enlarged view of W nanoprecipitates), and (b) high-resolution image of W precipitate.*

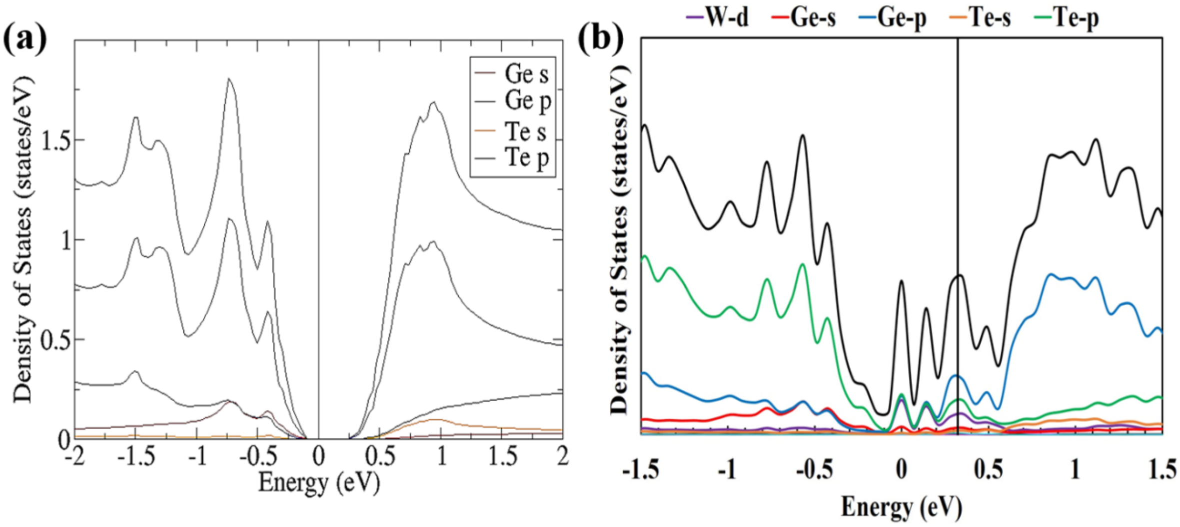

Figure S13. Electronic partial density of states (p-DOS) for (a) pristine GeTe, and (b) GeTe with interstitial W.

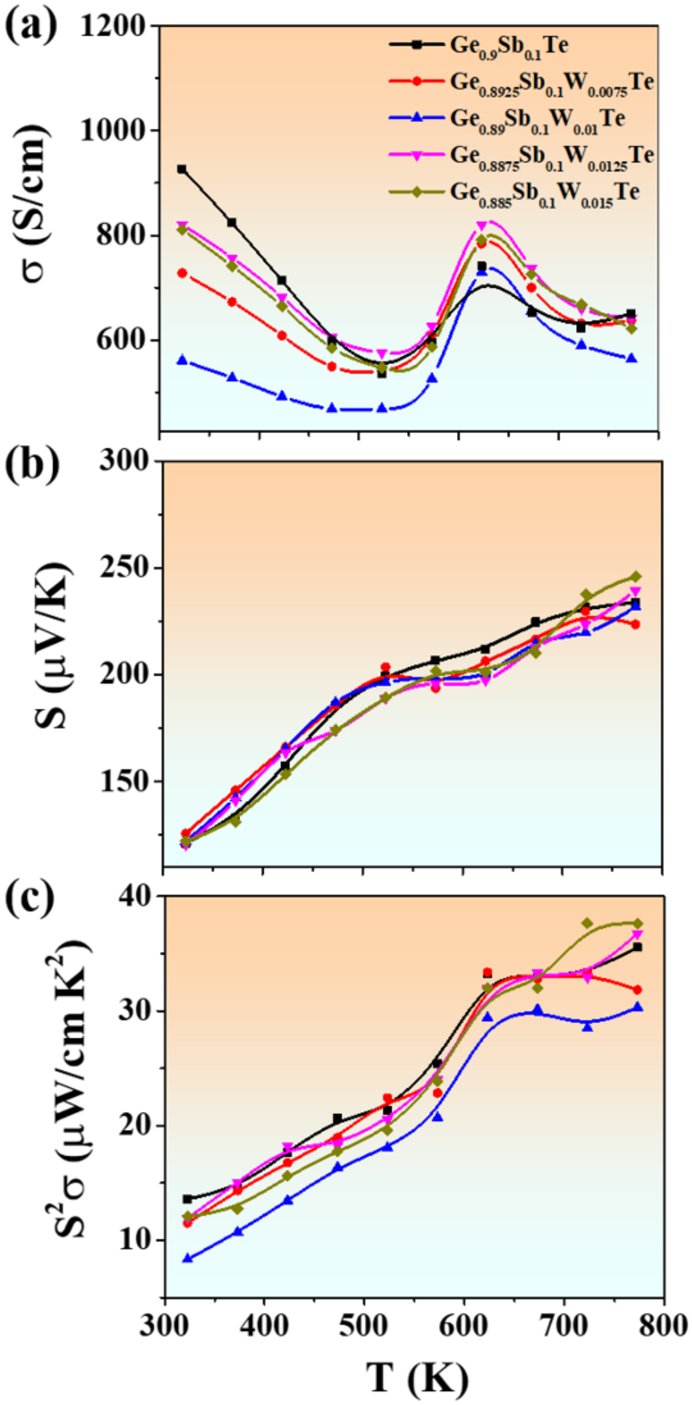

Figure S14.Temperature-dependent electronic transport properties of $Ge_{0.9-x}Sb_{0.1}W_xTe$ (x = 0.0075–0.015): (a) Electrical conductivity (σ), (b) Seebeck coefficient (S), and (c) power factor ($S^2σ$)

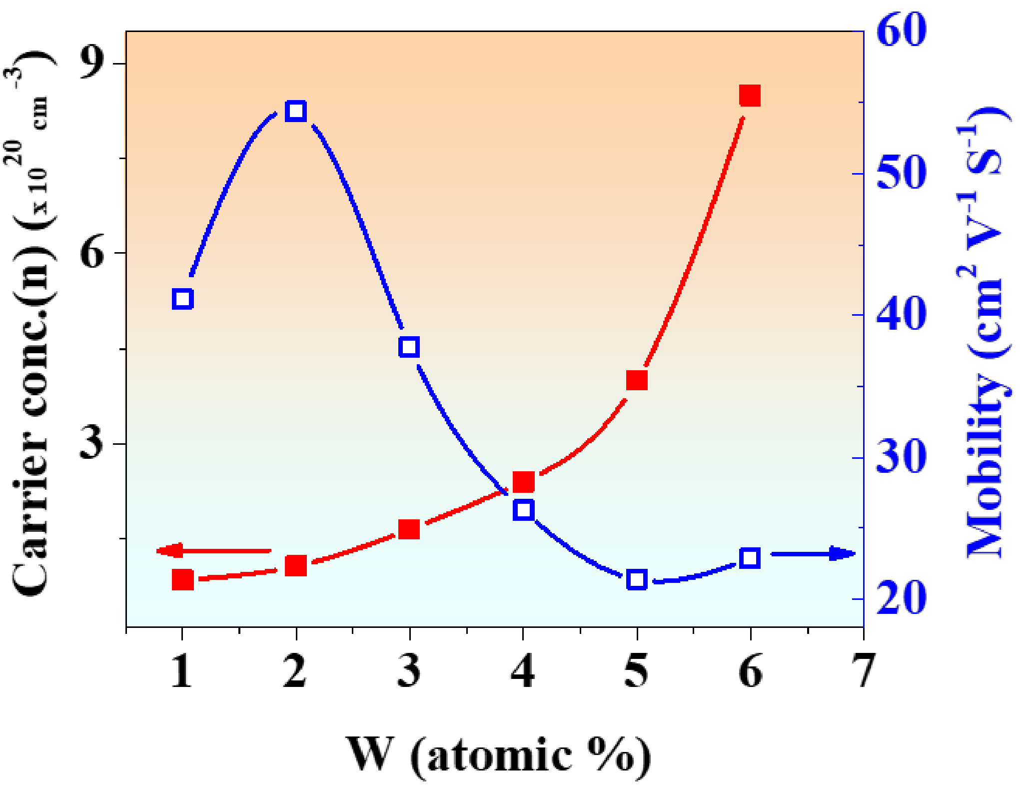

Figure S15. Composition-dependent carrier concentration (n) and mobility (μ) of $Ge_{0.9-x}Sb_{0.1}W_xTe$ *(x= 0.01–0.06).*

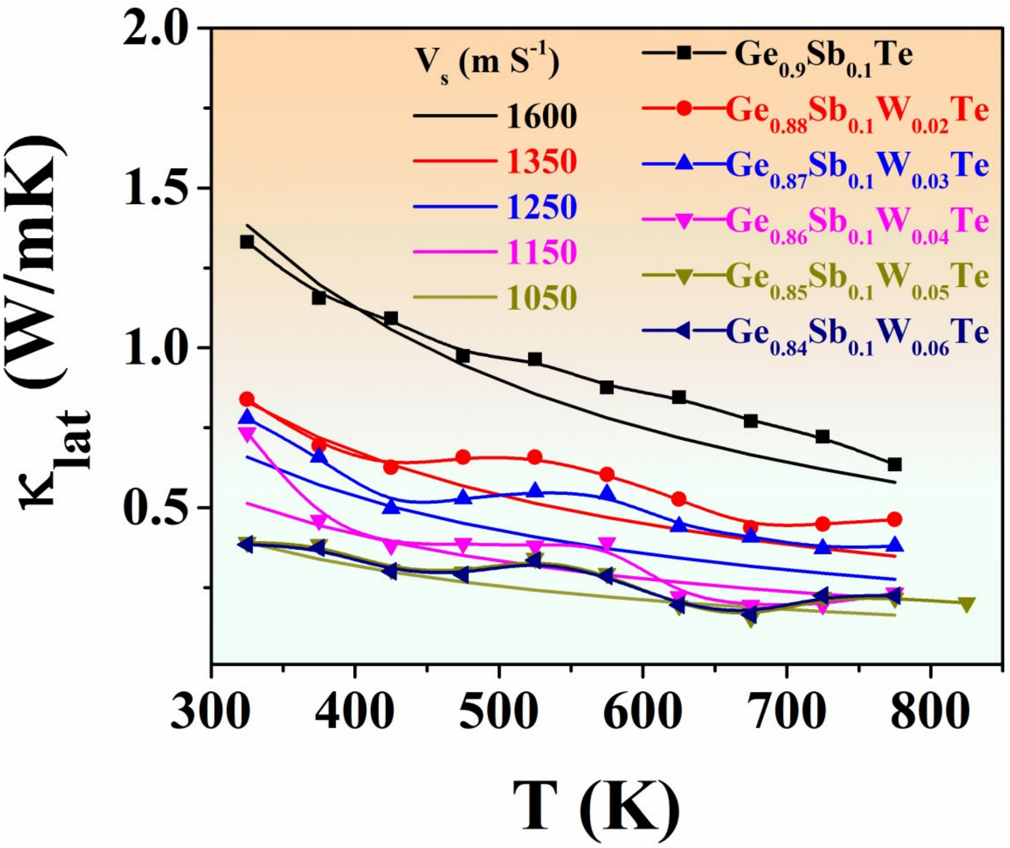

Figure S16. A reduction of κ_{lat} *upon the introduction of micro/nanostructural defects with increasing the W concentration. The lines show the* $\kappa_{lat} = Av_s^3T^{-1}$ *model*[7] *describing phonon thermal conductivity in the high-T limit at different velocity of sounds* (v_s) *where the only scattering mechanism is phonon–phonon scattering.*

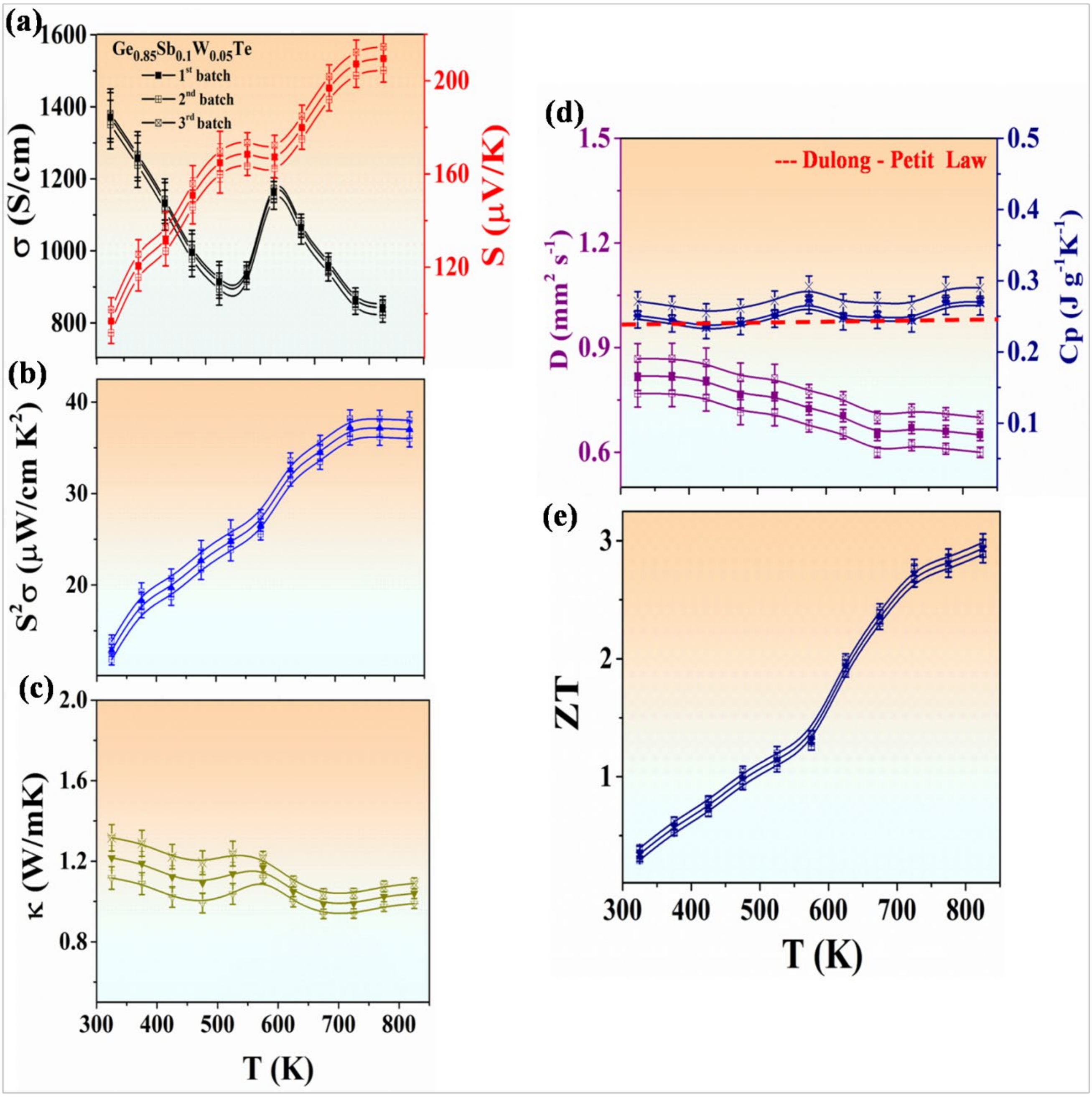

Figure S17. Reproducibility checking for the 3 batch of the $Ge_{0.85}Sb_{0.1}W_{0.05}Te$ samples with heating and cooling cycles error bar limit, (a) electrical conductivity (σ) and Seebeck (S), (b) power factor, (c) total thermal conductivity, (d)thermal diffusivity (D) and specific heat (Cp), and (e)Figure of merit (ZT).

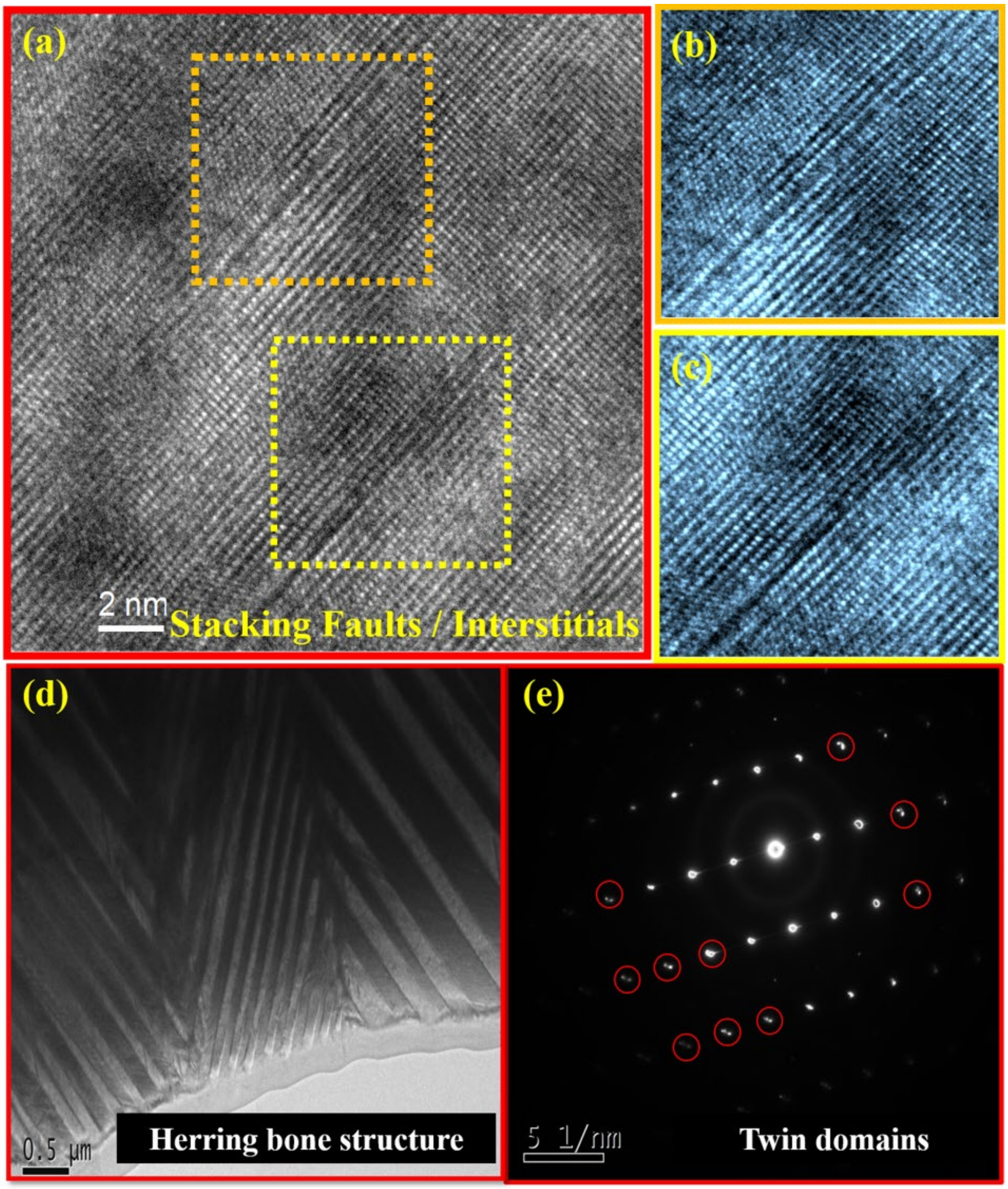

Figure S18. (a) Stacking faults of $Ge_{0.85}Sb_{0.1}W_{0.05}Te$ *indexed in square boxes; (b, c) magnified view of the stacking faults. (d) Herringbone structure of* $Ge_{0.85}Sb_{0.1}W_{0.05}Te$*, and (e) corresponding SAED pattern (inset, yellow circles represent twin domain structures)*

Highly doped GeTe showed many defects in the system owing to strain generated by the doped atoms, such as stacking faults, line defects, and vacancy layer formation. **Figure S18(a)** shows that defected stacking faults and a highly displaced lattice order was present, which might be due to the presence of W interstitials. **Figure S18(b)** shows a magnified view of the stacking fault present in compound $Ge_{0.85}Sb_{0.1}W_{0.05}Te$, while **Figure S18(c)** shows nonuniform lattice displacement formation, which was due to interstitial W atoms, as further confirmed in the following discussion. **Figure S18(d)** shows the herringbone structure of compound $Ge_{0.85}Sb_{0.1}W_{0.05}Te$ containing clear twin boundaries of white and dark colour domains along the distorted cubic (110) and (111) planes[11, 12]. **Figure S18(e)** shows the selective area electron diffraction (SAED) pattern for compound $Ge_{0.85}Sb_{0.1}W_{0.05}Te$, which clearly demonstrated the highly crystalline nature of the sample. The white dots in the SAED pattern were split, showing that the twin domain nature caused by the strain-induced domain boundaries of the herringbone structure was retained[11]. **Figure S11** shows a greatly enlarged image of the strained domain, with significant variation in the lattice architecture. These lattice disorders, point defects (Ge/Sb/W), and stacking faults provide plenty of opportunity for the whole phonon spectrum to disperse. **Figure S12(a)** shows the presence of W nanoprecipitates in the W-codoped samples, with the inset showing that the estimated nanoprecipitate size was around 10–20 nm. **Figure S12(b)** shows that the high-resolution W nanoprecipitates with an estimated size of 10–20 nm created strain along the $Ge_{0.85}Sb_{0.1}W_{0.05}Te$ lattice. TEM microstructural strain analysis confirmed that W was present in three forms, as follows: (i) <2 atom% W doped into Ge sites (as shown in **Figure S3(b)**), (ii) W existing in the form of interstitials owing to large changes in the lattice displacement (as shown in **Figure S18**), and (iii) leftover W forming nanoprecipitates with sizes of 10–20 nm (as shown in **Figure 3**).

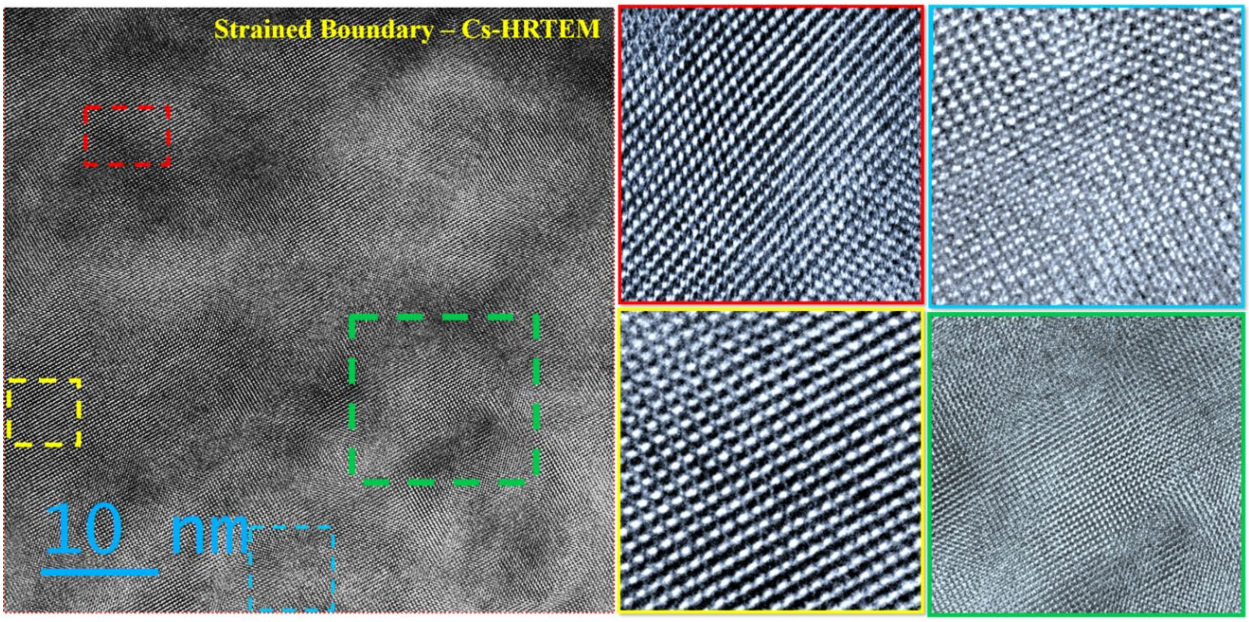

Figure S19:

Figure S19. Double Cs-corrected HR-TEM image of highly disordered strained boundary. Different colour boxes represent different atomic arrangements, and the green box represents W nanoprecipitation.

Figure S19 shows the double Cs corrected HR-TEM image of the $Ge_{0.85}Sb_{0.1}W_{0.05}Te$ sample to confirm the highly disordered boundary region. The strains present in the domain will be released at each end of the herringbone domain. These grain boundaries are stored with a huge strain, which will cause large atomic disorder. These lattice dynamic fluctuations resulting from different groups of atoms makes the lattice crystalline and partially liquid or disordered (amorphous)[13, 14]. High-resolution images with different atomic arrangement have been recorded and highlighted using different colours (yellow, red, green, and blue). A magnified view clearly showed that atomic disorder was present in the domain boundary (green box represents W-precipitated lattice with strain-surrounded lattice disorder).

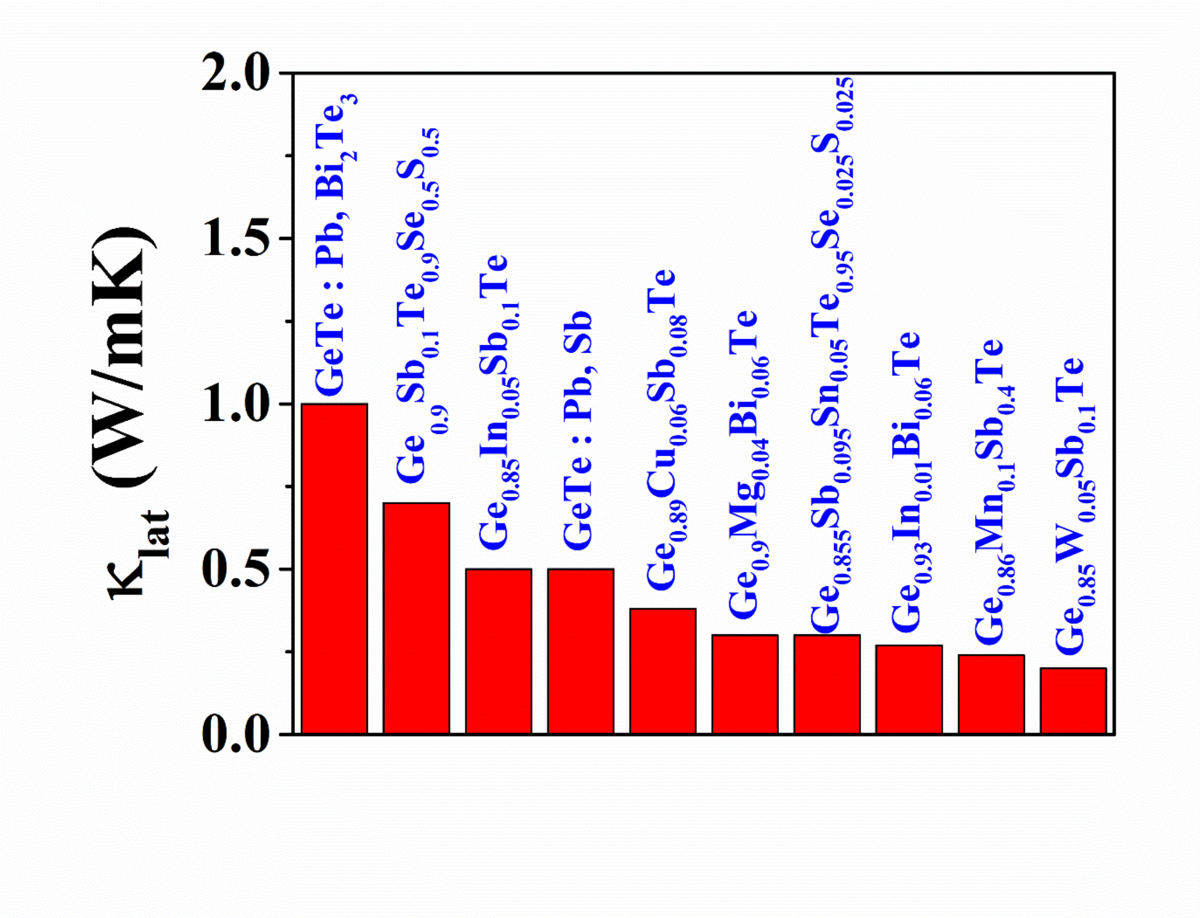

Figure S20: Lattice thermal conductivity (κ_{lat}) of GeTe based compounds.

References:

1. E. Levin, M. Besser and R. Hanus, *Journal of Applied Physics*, 2013, **114**, 083713.
2. I. N. Chen, C. W. Chong, D. P. Wong, L. M. Lyu, W. L. Chien, R. Anbalagan, M. Aminzare, Y. F. Chen, L. C. Chen and K. H. Chen, *physica status solidi (a)*, 2016, **213**, 3122-3129.
3. K. Ding, F. Rao, M. Xia, Z. Song, L. Wu and S. Feng, *Journal of Alloys and Compounds*, 2016, **688**, 22-26.
4. K. A. Cooley and S. E. Mohney, *Journal of Vacuum Science & Technology A: Vacuum, Surfaces, and Films*, 2019, **37**, 061510.
5. C. Peng, F. Rao, L. Wu, Z. Song, Y. Gu, D. Zhou, H. Song, P. Yang and J. Chu, *Acta Materialia*, 2014, **74**, 49-57.
6. S. Guo, Z. Hu, X. Ji, T. Huang, X. Zhang, L. Wu, Z. Song and J. Chu, *RSC Advances*, 2014, **4**, 57218-57222.
7. R. Hanus, M. T. Agne, A. J. Rettie, Z. Chen, G. Tan, D. Y. Chung, M. G. Kanatzidis, Y. Pei, P. W. Voorhees and G. J. Snyder, *Advanced Materials*, 2019, **31**, 1900108.
8. G. Wang, J. Zhou and Z. Sun, *Journal of Physics and Chemistry of Solids*, 2020, **137**, 109220.
9. K. S. Bayikadi, R. Sankar, C. T. Wu, C. Xia, Y. Chen, L.-C. Chen, K.-H. Chen and F.-C. Chou, *Journal of Materials Chemistry A*, 2019, **7**, 15181-15189.
10. J.-J. Kim, K. Kobayashi, E. Ikenaga, M. Kobata, S. Ueda, T. Matsunaga, K. Kifune, R. Kojima and N. Yamada, *Physical review B*, 2007, **76**, 115124.
11. K. S. Bayikadi, C. T. Wu, L.-C. Chen, K.-H. Chen, F.-C. Chou and R. Sankar, *Journal of Materials Chemistry A*, 2020, **8**, 5332-5341.
12. T. Xing, C. Zhu, Q. Song, H. Huang, J. Xiao, D. Ren, M. Shi, P. Qiu, X. Shi and F. Xu, *Advanced materials*, 2021, 2008773.
13. S. Zhao, Z. Li, C. Zhu, W. Yang, Z. Zhang, D. E. Armstrong, P. S. Grant, R. O. Ritchie and M. A. Meyers, *Science Advances*, 2021, **7**, eabb3108.
14. M. K. Jana and K. Biswas, *ACS Energy Letters*, 2018, **3**, 1315-1324.